IMAGING THE BLACK HOLE SILHOUETTE OF M87:
IMPLICATIONS FOR JET FORMATION AND BLACK HOLE SPIN

Avery E. Broderick[1] & Abraham Loeb[2]
Draft version December 1, 2008

ABSTRACT

The silhouette cast by the horizon of the supermassive black hole in M87 can now be resolved with the emerging millimeter very-long baseline interferometry (VLBI) capability. Despite being $\sim 2 \times 10^3$ times farther away than Sgr A* (the supermassive black hole at the center of the Milky-Way and the primary target for horizon-scale imaging), M87's much larger black hole mass results in a horizon angular scale roughly half that of Sgr A*'s, providing another practical target for direct imaging. However, unlike Sgr A*, M87 exhibits a powerful radio jet, providing an opportunity to study jet formation physics on horizon scales. We employ a simple, qualitatively correct force-free jet model to explore the expected high-resolution images of M87 at wavelengths of 1.3 mm and 0.87 mm (230 GHz and 345 GHz), for a variety of jet parameters. We show that future VLBI data will be able to constrain the size of the jet footprint, the jet collimation rate, and the black hole spin. Polarization will further probe the structure of the jet's magnetic field and its effect on the emitting gas. Horizon-scale imaging of M87 and Sgr A* will enable for the first time the empirical exploration of the relationship between the mass and spin of a black hole and the characteristics of the gas inflow/outflow around it.

Subject headings: black hole physics — techniques: interferometric — submillimeter — galaxies: active — galaxies: jets

1. INTRODUCTION

With the advent of millimeter VLBI, for the first time it has become possible to resolve the horizon of a black hole (Doeleman et al. 2008a; Doeleman 2008). Most of the theoretical and observational efforts on this front have been directed towards imaging Sagittarius A* (Sgr A*), the radio source associated with the supermassive black hole at the center of the Milky Way (see, e.g., Falcke et al. 2000; Broderick & Loeb 2005, 2006a,b; Miyoshi et al. 2007; Doeleman et al. 2008a). This is because Sgr A* subtends the largest angle of any known black hole candidate (roughly 55μas in diameter). Nevertheless, there is at least one other promising target for millimeter VLBI imaging, namely M87's supermassive black hole (hereafter labeled 'M87' for brevity).

At a distance of 16 Mpc and with a black hole mass of $3.4 \times 10^9 M_\odot$, the apparent diameter of M87's horizon is approximately 22μas, appearing about half as large as Sgr A*. Like Sgr A*, M87 is many orders of magnitude under-luminous in comparison to its Eddington luminosity. However, M87 is different from Sgr A* in five important respects.

First, M87 is located in the Northern sky, and thus is more amenable to imaging by telescope arrays comprised of existing millimeter and submillimeter observatories, which exist primarily in the Northern hemisphere. Thus, observations of M87 will generally have lower atmospheric columns and longer observing opportunities. Arrays of existing telescopes (see §2 for details), spanning projected baselines of 10^4 km, are already sufficient to resolve the silhouette at 1.3 mm (230 GHz) and 0.87 mm (345 GHz) with beam sizes of 17μas and 11μas, respec-

tively, along the minor axis. The inclusion of new facilities over the next few years will improve baseline coverage substantially, resulting in a roughly circular beam with these resolutions.

Second, M87's mass implies a dynamical timescale of roughly 5 hr, and a typical orbital timescale at the innermost-stable orbit of 2-18 days, depending upon the black hole spin. Thus, unlike Sgr A*, the structure of M87 may be treated as fixed during an entire day, one of the underlying assumptions of Earth aperture synthesis. This means that it will be possible to produce sequences of images of dynamical events in M87, occuring over many days.

Third, M87 exhibits a powerful jet, providing a unique opportunity to study the formation of relativistic jets on horizon scales. Realistic *ab initio* computations of jet formation are not presently possible, requiring jet simulations to make a variety of assumptions about the underlying plasma processes. Examples include assumptions about the dissipation scale, cooling rate, jet mass-loading mechanism, acceleration of the observed non-thermal electrons and even the applicability of the magnetohydrodynamic (MHD) prescription (De Villiers et al. 2003; McKinney & Gammie 2004; Komissarov 2005; McKinney 2006; Hawley & Krolik 2006; Tchekhovskoy et al. 2008; Igumenshchev 2008; Nishikawa et al. 2005). Thus, horizon-resolving images of M87's jet will critically inform our understanding of the formation, structure and dynamics of ultra-relativistic outflows.

Fourth, unlike Sgr A*, one is primarily driven towards submillimeter wavelengths by resolution requirements. There is no evidence for an analogous interstellar scattering screen that would blur high resolution images of M87 (cf. Bower et al. 2006). Nor is there evidence that M87 is optically thick at or about millimeter wavelengths (cf. Broderick & Loeb 2006a,b). Thus, modeling and interpreting images of M87 is likely to be somewhat more

[1] Canadian Institute for Theoretical Astrophysics, 60 St. George St., Toronto, ON M5S 3H8, Canada; aeb@cita.utoronto.ca
[2] Institute for Theory and Computation, Harvard University, Center for Astrophysics, 60 Garden St., Cambridge, MA 02138.

straightforward.

Fifth, despite being under-luminous, M87 is similar to other radio-loud quasars. The same cannot be said of Sgr A*, which is nearly dormant and is visible only due to its extraordinary proximity. As such, the faint low-mass black hole in Sgr A* is much more representative of the population of black holes that are accessible to the *Laser Interferometer Space Antenna* (LISA [3]). Careful comparison between horizon-scale imaging of Sgr A* and M87 will be crucial as a touchstone for comparing the astrophysical properties of these two populations, and how the black hole mass and spin affect the electromagnetic and kinetic properties of the surrounding plasma.

It is not surprising, therefore, that already high-resolution images of M87 has been aggressively pursued. The best known of these are the 7 mm VLBI images obtained by Junor et al. (1999) (and more recently by Ly et al. 2004; Walker et al. 2008). 3 mm and 2 mm images have also been reported (Krichbaum et al. 2006; Kovalev et al. 2007). These represent the highest resolution observations of a relativistic jet ever produced, probing down to roughly 5 Schwarzschild radii. Nevertheless, they are presently insufficient to directly address many outstanding questions in jet-formation theory. Among these questions are the role of the black hole spin in jet production, the structure of the jet forming region, the importance of magnetic fields and the particle content of the jet itself. However, all of these uncertainties may be settled by pushing to submillimeter wavelengths. In this sense, millimeter imaging promises to provide a qualitative change, not simply an incremental improvement. The reason for this is simple: the minimum relevant physical scale for a black hole of mass M is GM/c^2, and thus resolving this scale provides full access to the physical processes responsible for jet formation and accretion. In addition, the observation of the characteristic silhouette associated with the black hole settle the present ambiguity in identifying its position relative to the observed radio core (Marscher et al. 2008).

Motivated by the above arguments, we present in this paper predicted theoretical images of M87 for a class of force-free jet models which fit all existing observations. In particular, we assess the ability of possible millimeter & submillimeter VLBI experiments to distinguish different critical jet parameters. In §2 we review how a millimeter array can be created out of existing telescopes. In §3 we describe the jet-disk model we employ for M87. In §4 and §5 we present images and polarization maps, respectively, for a variety of jet models. Finally, §6 summarizes our main conclusions.

2. POTENTIAL MILLIMETER ARRAYS

A detailed discussion of existing telescopes that may serve as stations in a millimeter/submillimeter Very-Long Baseline Array (VLBA) can be found in Doeleman et al. (2008b). These facilities are: CARMA in Cedar Flat, California; the SMTO on Mount Graham, Arizona; the LMT on Sierra Negra, Mexico; APEX & ASTE, soon to be followed by ALMA, on the Atacama plane in Chile; the IRAM dish on Pico Veleta (PV), Spain; the IRAM Plateau de Bure (PdB) array in France; and a number of telescopes atop Mauna Kea, including the JCMT, SMA
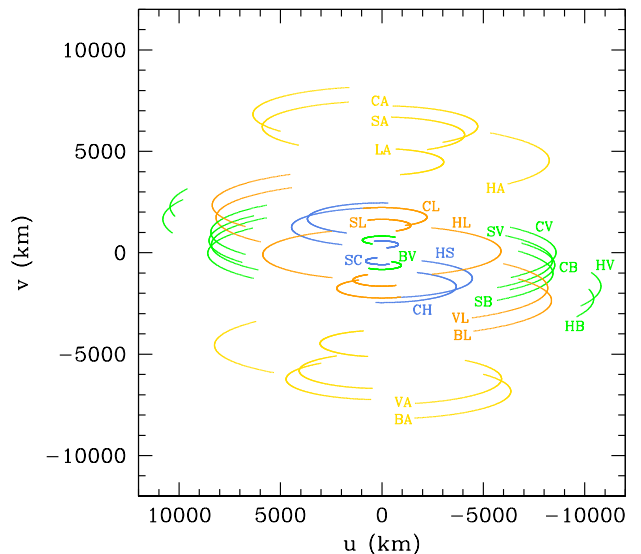
FIG. 1.— Tracks in the u-v plane (representing the Fourier-transform coordinates of the sky) made as the Earth rotates by existing and forthcoming telescopes as seen by M87. Blue tracks are associated solely with the existing North American telescopes (SMA, JCMT, CARMA & SMTO), green includes the two European observatories (PdB & PV), orange includes the LMT and yellow includes telescopes in Chile (APEX & ALMA). The tracks are labelled according to H (CSO, SMA, JCMT), C (CARMA), S (SMTO), B (PdB), V (PV), L (LMT) and A (APEX, ASTE, ALMA).

and CSO, that may be used independently or phased together to provide single Hawaiian station. The millimeter flux from M87 is a factor of 2–3 lower than Sgr A*, and thus telescope sensitivity will be a key factor in resolving small-scale structure. This may be achieved in a variety of ways, including phasing together the individual telescopes in the CARMA, ALMA, SMA and PdB into single apertures at their respective locations. In addition, a shift to large-bandwidths will likely be required.

As mentioned in §1, M87 has a number of observational advantages over Sgr A*, the primary one being its location in the Northern sky. This is evident in the baseline coverage provided by the previously mentioned telescopes, shown in Fig. 1. M87 is simultaneously visible at the European stations (PV and PdB) and the North American stations (Hawaii, CARMA and SMTO). With the inclusion of the LMT, the baseline coverage is nearly complete within a narrow, roughly East-West ellipse, providing a resolution in this direction of approximately $17\,\mu$as and $11\,\mu$as at 1.3 mm and 0.87 mm, respectively. Introducing a station in Chile results in a similar resolution along the North-South direction.

Critical for Earth aperture synthesis, M87's substantially larger mass implies that it may be regarded as a stationary source, even on horizon scales, for timescales of order a day. The sparseness of the baseline coverage of Sgr A*, which varies over 15 min timescales, is due not only to the limited number of existing stations, but also the fact that visibilities taken throughout the night cannot generally be assumed to arise from the same in-
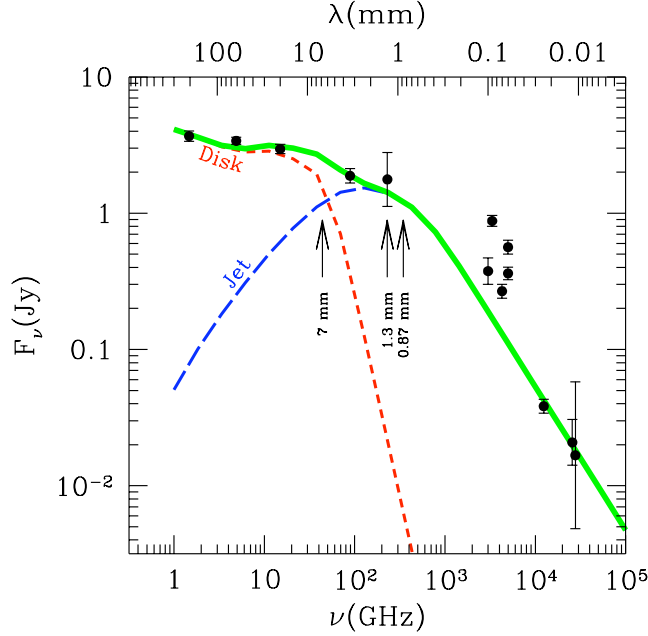
FIG. 2.— Spectra of our canonical jet-disk model. The disk & jet components are shown by the short-dashed, red line and the long-dashed, blue line, respectively. The total spectrum is shown by the thick green line. Data points are collected from Biretta et al. (1991); Despringre et al. (1996); Perlman et al. (2001, 2007); Tan et al. (2008). The errors on the data points represent the instrumental uncertainty, not the variability, and thus are an underestimate for the multi-epoch SED. The spectra of the other jet-disk models are nearly indistinguishable from the one shown.

trinsic brightness distribution. Thus, in the absence of additional telescopes, efforts to interpret features in the image of Sgr A* (such as a black hole silhouette, Mills 1962), will need to be performed in Fourier space. In contrast, M87's comparably long dynamical timescale means that images can be produced and analyzed directly. This is even true during dynamical periods in which the accretion flow is changing as rapidly as it can around the horizon.

3. MODELING M87

There are a number of observational constraints upon any model for M87. Foremost among these is the observed Spectral Energy Distribution (SED), shown in Fig. 2, exhibiting a nearly flat, but not inverted, radio spectrum and a steep non-thermal decline from millimeter to infrared wavelengths. It is important to note that there is no contemporaneous measurement of M87's SED from the radio to the infrared, the points shown in Fig. 2 having been collected over nearly two decades. The error bars shown represent the instantaneous measurement errors, and are considerably smaller than the observed variability. Further difficulties arise in isolating the "nuclear" emission, that arising in the vicinity of the black hole, from the emission due to knots in the parsec-scale structure of the jet and dust in the nucleus of the surrounding galaxy. This latter effect is especially problematic between 24 and 100 microns (3×10^3–10^4GHz), where the SED is dominated by nuclear dust emission (Perlman et al. 2007). For this reason, we do not attempt to fit the SED at these wavelengths.

In addition to the SED, there are a number of 7 mm

VLBA images, showing the beginnings of the jet on milliarcsecond scales (Junor et al. 1999; Ly et al. 2004; Walker et al. 2008). Any viable model for M87 must be able to reproduce this extended 7 mm emission, and in particular showing the wide jet morphology.

In Eddington units, M87 is significantly underluminous for an accreting black hole, though considerably more luminous than a rescaled Sgr A*. This may be in part due to the presence of a jet. However, a number of authors have found that M87's SED is best fit by a two-component model consisting of a Radiatively Inefficient Accretion Flow (RIAF)-type disk producing the flat radio spectrum, and a jet producing the millimeter, infrared and optical spectrum (Yuan 2000; Reynolds et al. 1999). The requirement that these models be able to qualitatively reproduce the 7 mm VLBA image implies that the jet luminosity must be comparable to, if not dominate, that from the disk component at this wavelength. In the following subsections we describe our models for the disk and jet structures, their emission and our effort to fit all observational constraints simultaneously.

3.1. Radiative Transfer

The primary emission mechanism is synchrotron, arising from both thermal and non-thermal electrons. We model the emission from the thermal electrons using the emissivity described in Yuan et al. (2003), appropriately altered to account for relativistic effects (see, e.g., Broderick & Blandford 2004). Since we perform polarized radiative transfer via the entire complement of Stokes parameters, we employ the polarization fraction for thermal synchrotron as derived in Petrosian & McTiernan (1983). In doing so we have implicitly assumed that the emission due to thermal electrons is isotropic, but this simplifying assumption is not expected to affect our results significantly.

Regarding the non-thermal electrons, we follow Jones & Odell (1977) in assuming a power-law electron distribution with a cut-off below some minimum Lorentz factor. As shown below, the corresponding low-frequency cut-off is critical to fitting M87's millimeter spectrum. For both thermal and non-thermal electrons, the absorption coefficients are determined directly via Kirchoff's law (Broderick & Blandford 2004).

3.2. Disk

Given the low core luminosity of M87 in Eddington units, we employ a radiatively-inefficient accretion flow model similar to the one we have previously used for Sgr A* (Broderick & Loeb 2006a; Broderick et al. 2008). This model is adequate at the low accretion rate of interest here and makes use of the homologous nature of black hole accretion flows. Furthermore, this model incorporates, in a limited sense, the presence of outflows, clearly appropriate for M87. Unlike Sgr A*, M87's radio spectrum is not inverted, and so the model parameters are different. It is important to emphasize that our images are largely insensitive to the particular model we adopt for M87's accretion flow, since at millimeter wavelengths M87 is dominated by the jet emission. Thus, while we include a disk model for completeness, alternative accretion models produce nearly identical results at millimeter wavelengths.
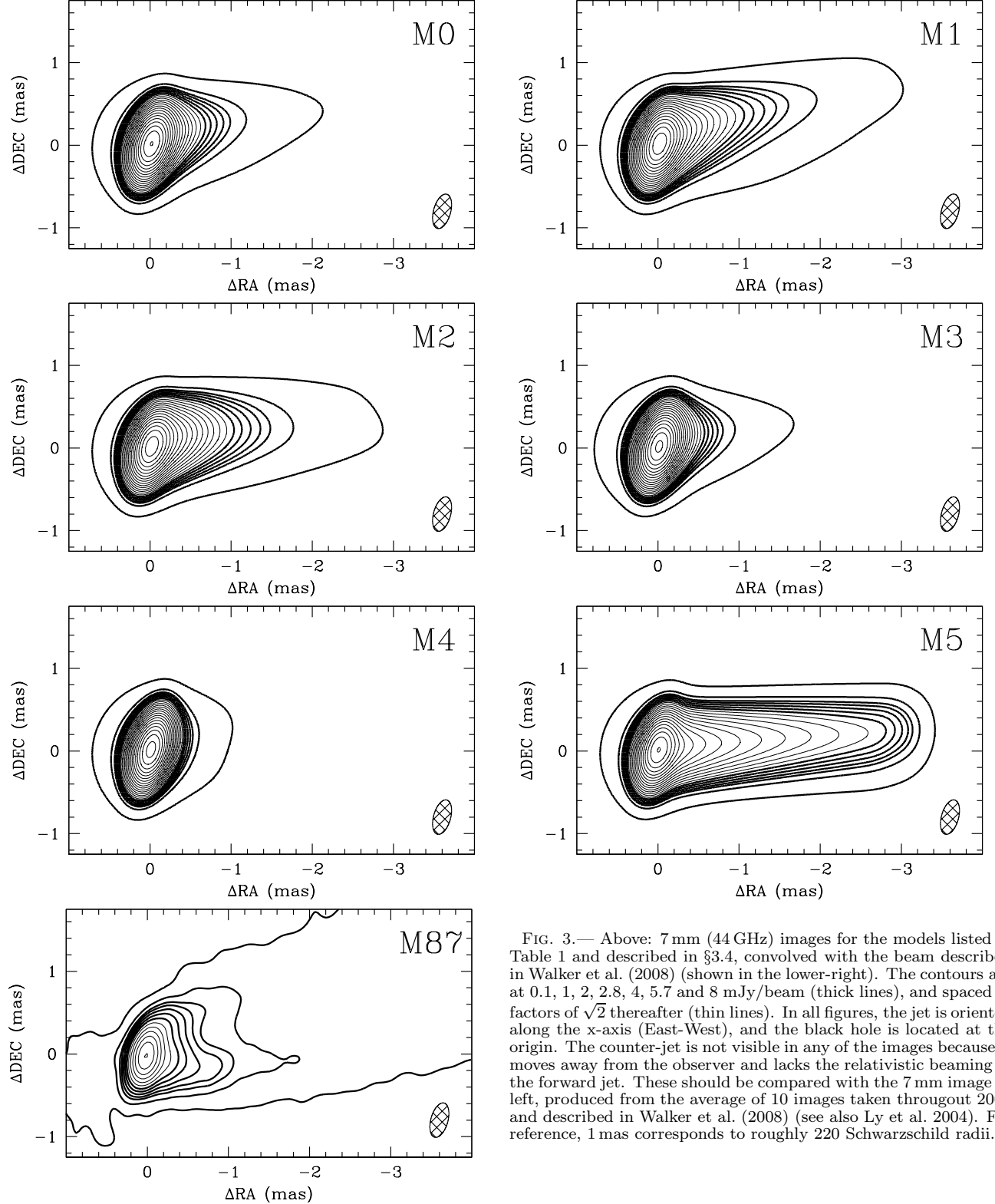
FIG. 3.— Above: 7 mm (44 GHz) images for the models listed in Table 1 and described in §3.4, convolved with the beam described in Walker et al. (2008) (shown in the lower-right). The contours are at 0.1, 1, 2, 2.8, 4, 5.7 and 8 mJy/beam (thick lines), and spaced in factors of $\sqrt{2}$ thereafter (thin lines). In all figures, the jet is oriented along the x-axis (East-West), and the black hole is located at the origin. The counter-jet is not visible in any of the images because it moves away from the observer and lacks the relativistic beaming of the forward jet. These should be compared with the 7 mm image at left, produced from the average of 10 images taken througout 2007 and described in Walker et al. (2008) (see also Ly et al. 2004). For reference, 1 mas corresponds to roughly 220 Schwarzschild radii.

In our model, the accreting plasma is characterized by both thermal and non-thermal populations of electrons. Both of these are dynamically unimportant, with the underlying ions providing the dominant pressure and determining the magnetic field strength. The particle densities are taken to be broken power laws, with a break at some radius R_b which was subsequently adjusted to fit the radio spectrum cut-off, making this qualitatively similar to the truncated disk solutions discussed by Yuan (2000). Outside of R_b, the power law indicies of the thermal particles were taken from Yuan et al. (2003), leaving only the normalizations to be adjusted. To fit the radio spectral index, we also modified the radial dependence of non-thermal particles.

Specifically, the density of the thermal electrons is given by

$$n_{th} = n_{th,0}\,e^{-z^2/2R^2} \begin{cases} (r/R_b)^{-0.7} & \text{if } r \geq R_b \\ 1 & \text{otherwise.} \end{cases} \quad (1)$$

where z is the height, R is the cylindrical radius, and $r = \sqrt{z^2 + R^2}$. The thermal electron temperatures is given by

$$T_e = T_{e,0}\,(r/R_b)^{-0.84}\,, \quad (2)$$

which is different from the ion temperature, assumed to be at the virial value. The corresponding magnetic field strength is determined via

$$\frac{B^2}{8\pi} = \beta^{-1} n_{th} \frac{m_p c^2}{6r}\,, \quad (3)$$

and oriented toroidally, where all lengths are measured in units of GM/c^2. In all models, $\beta = 10$.

Similarly, the non-thermal electron density is given by

$$n_{nth} = n_{nth,0}\,e^{-z^2/2R^2} \begin{cases} (r/R_b)^{-2} & \text{if } r \geq R_b \\ 1 & \text{otherwise,} \end{cases} \quad (4)$$

where the radial power-law index was chosen to roughly reproduce the radio spectrum. The associated spectral index is 3 (i.e., the spectral flux of the optically thin disk scales with frequency ν as $F_\nu \propto \nu^{-3}$). The minimum Lorentz factor was set to 100, in approximate agreement with Yuan et al. (2003). Finally, the disk velocity was assumed to be Keplerian outside of the Innermost Stable Circular Orbit (ISCO), and to follow ballistic plunging inside the ISCO.

As discussed in §3.4, qualitatively reproducing the 7 mm observations of Sgr A* requires the disk to become subdominant by this wavelength. We found that this requires $R_b \simeq 20\,GM/c^2$. The normalizations for the thermal electrons are $n_{th,0} = 1.23 \times 10^4\,\text{cm}^{-3}$ and $T_{e,0} = 8.1 \times 10^9\,\text{K}$. The normalization for the non-thermal electron density depends upon the particular model being considered (see Table 1). For the case where the disk is viewed from 40° from the jet-axis, we set $n_{nth,0} = 6.1 \times 10^2\,\text{cm}^{-3}$, while for all other cases $n_{nth,0} = 3.8 \times 10^2\,\text{cm}^{-3}$. Note that for all models, the non-thermal electron density is substantially lower than its thermal counterpart.

The associated disk spectrum is shown by the red, short-dashed line in Fig 2. As required, it becomes subdominant near 7 mm, and completely negligible by 1 mm. For this reason, the particular details of the disk modeling are unlikely to affect the millimeter wavelength images of M87's jet.

3.3. Magnetically Dominated Jet

Any viable jet model must satisfy a variety of theoretical considerations. These include providing a qualitatively realistic relationship between the acceleration and collimation, the presence of helical motion, the conversion from a poloidally dominated magnetic field to a toroidal magnetic field at large distances, and a transition from a jet to a trans-relativistic disk wind at large values of the cylindrical radius. Finally, any such model must be numerically well behaved everywhere.

In practice, all of these conditions could be met by appropriating the output of recent jet-formation simulations (e.g., Tchekhovskoy et al. 2008; Igumenshchev 2008; McKinney 2006; Hawley & Krolik 2006; Nishikawa et al. 2005). While this approach will undoubtedly prove productive in the future, it is poorly suited to the goals of this investigation. Presently, despite being self-consistent, simulations are expensive, do not provide sufficiently fine-grained controls over the jet parameters and would not allow for comparisons outside the realm of MHD jets. In addition, there is considerable uncertainty regarding the mass-loading, critical to the creation of images. For these reasons, we opted to produce a qualitatively correct cartoon of magnetically dominated jets based upon force-free models of Tchekhovskoy et al. (2008), exhibiting many of the required properties but providing sufficient freedom to explore a variety of jet morphologies that may be outside of the purview of existing General Relativistic MHD simulations. Here we only summarize the physical reasoning and the final structure of the jet, leaving many of the details to the Appendix.

Numerical simulations suggest that outside of the accretion disk the plasma is magnetically dominated (see, e.g., McKinney 2006; Hawley & Krolik 2006). Thus, we model the outflow as stationary, axisymmetric and force-free. In such configurations, the magnetic field is described by a stream function, ψ, which must satisfy a 2nd-order partial-differential equation. A physically relevant approximate solution is

$$\psi = r^{2-2\xi}\,(1 - \cos\theta)\,. \quad (5)$$

For $0 < \xi < 1$, this solution is within 10% of the stream function inferred from existing numerical simulations (Tchekhovskoy et al. 2008). At large distances, $R \propto z^\xi$, and thus ξ defines the collimation rate. For $\xi = 0$ and $\xi = 1$, the jet is cylindrical and conical, respectively; a more typical value is $1/2$.

The structure of the magnetic field and the velocity of the outflow depend upon the angular velocity at the field-footprint, $\Omega(\psi)$, which is a function solely of ψ. The associated four-velocity is

$$u_F^\mu = u_F^t\,(1, 0, 0, \Omega(\psi))\,, \quad (6)$$

where u_F^t is determined via a normalization condition. Near the light cylinder this choice of u_F^μ transitions from time-like to space-like. There is no physical problem with this choice, meaning only that we have chosen a pathological observer. Thus, we choose $u_F^t > 0$ and set $\sigma = u_F^\mu u_{F\,\mu} = \pm 1$. At the light cylinder, this is ill-defined. However, as shown below, the plasma structure is continuous across this surface, and thus we simply interpolate across the light cylinder to obtain its characteristics at this position. We define $\Omega(\psi)$ in the equatorial

plane, choose it to be the Keplerian angular velocity outside of the ISCO, and fix it to the ISCO value inside. This boundary is usually what demarcates the "jet", separating it from the surrounding disk wind.

The stream function also defines the magnetic field structure. Within the u_F-frame (which we shall denote by the subscript F), the poloidal magnetic field 4-vector (see the Appendix for the definition in terms of the electromagnetic field tensor) is given by

$$b_F^r = -B_0 \frac{\sigma}{u_F^t \sqrt{-g}} \frac{\partial \psi}{\partial \theta} = -B_0 \sigma \frac{r^{2-2\xi} \sin\theta}{u_F^t \sqrt{-g}}$$
$$b_F^\theta = B_0 \frac{\sigma}{u_F^t \sqrt{-g}} \frac{\partial \psi}{\partial r} = B_0(2-2\xi)\sigma \frac{r^{1-2\xi}(1-\cos\theta)}{u_F^t \sqrt{-g}}$$

$$(7)$$

The toroidal magnetic field may be constructed by noting that $b_{F\phi}/u_F^t$ must be a function of ψ alone as well. Choosing this function amounts to choosing the current distribution within the outflow. However, the condition that the poloidal field dominates at large distances gives

$$b_{F\phi} = -2B_0 \Omega \psi u_F^t \,, \qquad (8)$$

where the minus sign arises from the fact that field lines are swept back by the motion of the accretion disk. Finally, b_F^t is obtained from the identity $u_F^\mu b_{F\mu} = 0$.

We assume that the plasma velocity is similar to the drift velocity as seen in the frame of a zero-angular momentum observer (ZAMO). This is equivalent to assuming that the plasma is not relativistic at the jet footprint within this frame; it gives

$$u^\mu = \gamma (u_F^\mu + \beta b_F^\mu) \qquad (9)$$

where

$$\gamma = -\frac{\sigma}{\sqrt{-(\sigma + \beta^2 b_F^2)}} \quad \text{and} \quad \beta = \frac{\sigma b_F^t}{b_F^2 u_F^t} \,. \qquad (10)$$

As shown in the Appendix, unlike u_F^μ this velocity is always time-like. The magnetic field 4-vector in the plasma frame is then

$$b^\mu = \gamma \left(b_F^\mu - \sigma \beta b_F^2 u_F^\mu \right) \,. \qquad (11)$$

All that remains is to define the mass content of the outflow. To do this properly would require a full understanding of the mass-loading and particle acceleration in jets, that presently does not exist. Therefore, we employ a simple, parametrized prescription based upon mass conservation. As shown in the Appendix, the particle density n satisfies in Boyer-Lindquist coordinates,

$$\frac{\gamma n}{u_F^t b_F^2} \left(g^{tt} + g^{t\phi}/\Omega \right) = F(\psi) \,, \qquad (12)$$

for an arbitrary function of the stream function. We choose the particular form of $F(\psi)$ by defining the jet density n on a slice at some height above the disk. Specifically, we chose the profile to be a Gaussian of the form $n \propto \exp\left(-r^2 \sin^2\theta/2r_{\rm fp}^2\right)$, at a height $|r\cos\theta| = r_{\rm fp}$. With b_F^μ, u_F^t and Ω known, this is sufficient to define $F(\psi)$ everywhere. Finally, this was supplemented with a cut-off for $r < r_{\rm fp}$, mimicking the loading of the jet above the black hole, yielding

$$n = n_0 \frac{u_F^t b_F^2 F(\psi)}{\gamma (g^{tt} + g^{t\phi}/\Omega)} \left(1 - e^{-r^2/2r_{\rm fp}^2} \right) \,. \qquad (13)$$

TABLE 1
JET MODEL PARAMETERS

Model	$a(M)$	θ	$r_{\rm fp}(GM/c^2)$	ξ
M0	0.998	25°	10	1/2
M1	0.998	25°	20	1/2
M2	0	25°	10	1/2
M3	0.998	40°	10	1/2
M4	0.998	25°	10	5/8
M5	0.998	25°	10	3/8

Again, we assume a minimum Lorentz factor of 10^2. In contrast to the disk, however, we choose a spectral index between 1.0 and 1.13, depending upon the particular model in Table 1.

In summary, the parameters that control the jet are the collimation rate, ξ, the footprint size, $r_{\rm fp}$, the magnetic field and density normalization, B_0 and n_0. The latter two are set by fitting M87's spectrum, leaving the first two unconstrained.

3.4. *Fitting Existing Constraints*

The two empirical constraints that we considered were M87's SED and the 7 mm VLBI images. These are not completely independent since, as alluded to earlier, the jet at 7 mm must be sufficiently bright to produce the extended emission that is observed in the VLBI images. Conversely, this requires that the disk become subdominant, and thus is the motivation behind the truncated disk. In addition, the cut-off in the spectrum due to the minimum Lorentz factor of the non-thermal jet electrons is critical to forcing the jet component of the spectrum to turn over near 1 mm, ensuring that it does not over-produce the flux at longer wavelengths.

The particular normalizations for the electron densities and magnetic fields in the disk and jet are determined by fitting the SED shown in Fig. 2. The disk component is shown by the red, short-dashed line and falls off rapidly near 7 mm. The jet component for our conical jet model (M0, Table 1) is shown by the blue, long-dashed line. This fits the millimeter–optical spectrum, and is dominated by the disk spectrum above 7 mm. Within this model there is some detailed balancing of the two components, which is presumably associated with the physics of jet formation.

Despite treating the disk and jet components independently, making no attempt to merge the two, we find that the jet magnetic field and the magnetic field in the inner part of the disk are quite similar, differing by factors of a few. In contrast, the jet density is typically considerably lower than disk densities, being an order of magnitude smaller than that of the non-thermal electrons in the disk. However, this disparity is consistent with jet simulations which have generally shown that it is quite difficult for disk material to diffuse onto the ordered field lines within the jet (McKinney & Gammie 2004; Komissarov 2005; De Villiers et al. 2005; McKinney 2006).

We consider six jet-disk models altogether, the parameters of which are listed in Table 1. These explore the dependence of the jet structure and images upon the variation of a single jet parameter at a time. The spectra for all models are nearly indistinguishable from that shown in Fig. 2. The 7 mm image, convolved with the beam reported in Walker et al. (2008) and Ly et al. (2004) (see
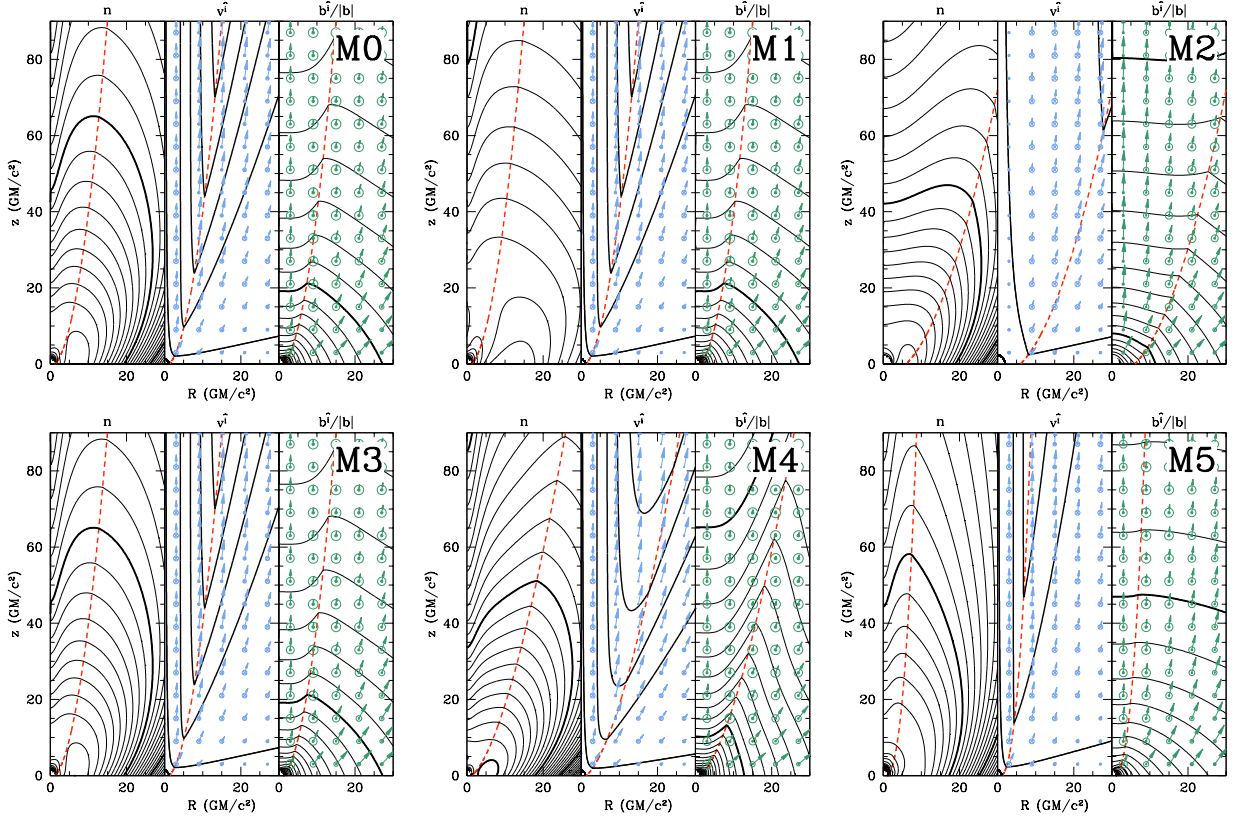
FIG. 4.— Density, velocity and magnetic structure for the jet models listed in Table 1. For each, the density is shown in the left panel with thin/thick contours for $\log{(n/n_{max})}$ in steps of 0.1/1. The velocity is shown in the center panel, $v^{\hat{i}} = \sqrt{g_{ii}} u^i / u^t$, with contours of the asymptotic Lorentz factor ($-u_t$) in steps of 1 (unit asymptotic Lorentz factor is shown by the lowest contour that extends across the entire range in R). The magnetic field structure is shown in the right panel. The contours denote the magnitude of the magnetic field in the plasma frame, and are distributed in the same fashion as the density contours. Due to the considerable change in magnitude over the range shown, the magnetic field direction is shown by the vector field, where $b^{\hat{i}} = \sqrt{g_{ii}} b^i$. For both the velocity and magnetic field plots, the toroidal and poloidal vectors are normalized relative to each other such that they are equal when the toroidal circle has a diameter equal to the length of the poloidal vector. In all panels, the magnetic field surface passing through the ISCO is shown by the dashed red line.

also Junor et al. 1999) is shown for each model in Fig. 3. Generally we find an acceptable qualitative agreement, which is not trivial given the dubious extension of the force-free jet model to these angular scales (corresponding to many hundreds of Schwarzschild radii). We note, however, that the brightness profile of our canonical jet model decreases much more rapidly ($\propto z^{-3}$) than that observed by Walker et al. (2008) ($\propto z^{-1.8}$), implying that corrections to our simplistic model are required far from the black hole. Indeed, because we don't model the instabilities and subsequent internal shocks noted in simulations, which ultimately redistribute the jet's magnetic and particle energy, our jet continues to accelerate, reaching unphysically large Lorentz factors by these angular scales. Nevertheless, we obtain roughly the correct morphology for the single jet orientation we consider, East-West.

The density, velocity and magnetic field structure, shown in Fig. 4 for the scale that dominates the millimeter images, share a number of common features. In all, the critical surface defined by that poloidal field line which passes through the ISCO, shown by the red dashed line, is associated with a qualitative change in the outflow. Following McKinney (2006), by "jet" we will refer the region inside this surface, and by "wind" we mean

the region outside. It is along this surface that the highest Lorentz factors are reached and the velocity is most poloidal (i.e., the velocity pitch angle is largest). As we move away from this surface, both within the jet and the wind, the toroidal velocity component increases. Conversely, the magnetic field is most toroidal (i.e., the magnetic pitch angle is smallest) along this surface, with an increasing poloidal component on both sides. Finally, the density generically reaches a maximum along this surface.

This behavior is not unexpected, deriving directly from the velocity of the magnetic field footprints. Outside of the ISCO, the footprint velocity is monotonically decreasing with radius (since Ω is set to the Keplerian value). Inside of the ISCO Ω is held fixed and thus the velocity is increasing with radius. Thus, the critical magnetic field surface corresponds to the maximum footprint velocity, with the jet and wind structure on either side roughly mirroring each other.

Next we discuss the individual model features separately.

3.4.1. M0

M0 represents our canonical jet model, having parameters that are are broadly consistent with numeri-
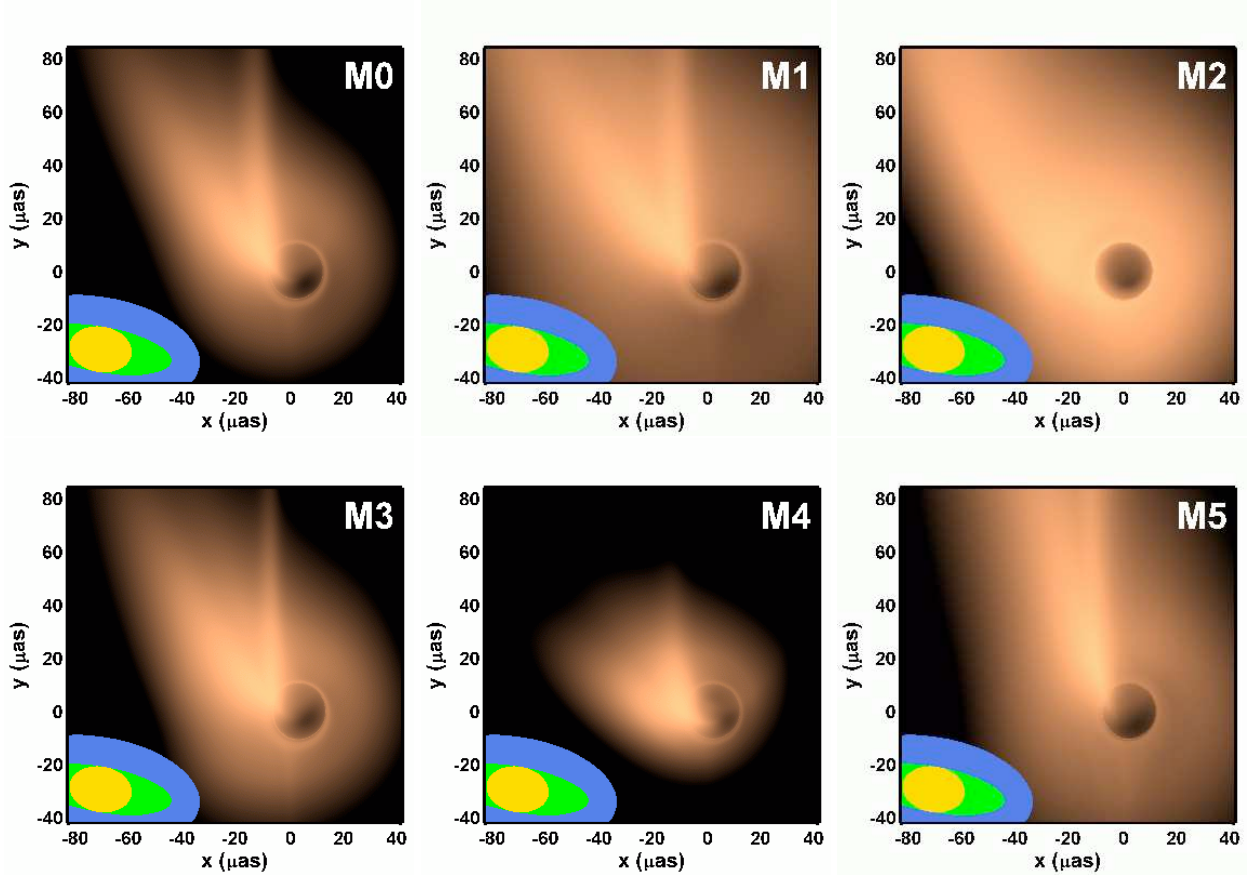
FIG. 5.— 1.3 mm (230 GHz) images for the models listed in Table 1 and described in §3.4. The brightness scale is logarithmic, showing a dynamic range of 128, similar to the existing 7 mm images. In all images the projected jet axis is parallel to the vertical axis. The ellipses in the lower left provide an estimate of the beam size for arrays consisting of the North American telescopes only (blue), including the European telescopes & the LMT (green), and all telescopes (yellow).

cal simulations and direct observations of M87. In this case the black hole is rapidly rotating, has a footprint of $r_{\rm fp} = 10GM/c^2$ and collimation index of $\xi = 1/2$. Spectra and images are produced by viewing the jet at $25°$ from the jet/spin axis, as inferred from observations of super-luminal knots (Heinz & Begelman 1997). The asymptotic Lorentz factor reaches 5 within the region shown in Fig. 4, and is comparable to that inferred in M87 (Heinz & Begelman 1997). This model easily produces the extended 7 mm emission, with the slight deviation from purely East-West orientation arising due to the helical motion of plasma in the jet.

3.4.2. *M1*

M1 is identical to M0, save for the increased footprint size, $r_{\rm fp} = 20$. This may be the case, e.g., if black hole spin does not play the central (anticipated) role in launching the jet. The velocity and magnetic field structures are identical to those of model M0, the only difference being the width of the density distribution. This has consequences for the normalizations of the density and magnetic field, with the larger geometric area forcing these to be substantially smaller in magnitude. Again, this model is qualitatively able to reproduce the 7 mm observations, perhaps even better than model M0.

3.4.3. *M2*

M2 corresponds to a jet from a non-rotating black hole. The primary consequence of setting $a = 0$ is to increase the ISCO radius, thus substantially decreasing the maximum footprint velocity and widening the critical magnetic surface. Thus, even with $r_{\rm fp} = 10$ and $\xi = 1/2$, as in M0, the jet appears considerably broader, and is accelerated much more slowly. In the region shown by Fig. 4, the maximum asymptotic Lorentz factor reached is only 2. Nevertheless, M2 is capable of producing the extended 7 mm emission that is observed.

3.4.4. *M3*

The structure of the jet in M3 is identical to M0, the only difference being the viewing angle. For M3, this is chosen to be $40°$ from the jet/spin axis. As a consequence, the density and magnetic normalizations of the jet and the underlying disk needed to be adjusted. Otherwise, there is no difference in the modelling.

3.4.5. *M4*

M4 is a moderately less collimated jet, with $\xi = 3/8$. This relatively small change in the collimation rate has dramatic consequences for the density and magnetic field structure, both falling off much more rapidly in this case. The shape of the asymptotic Lorentz factor contours are somewhat different from those associated with M0, exhibiting a more gradual transition between the jet and

wind regions. Nevertheless, the maximum asymptotic Lorentz factor reached is 5, similar to M0. In this case, the 7 mm image is considerably different than that of the previous models, appearing more compact due primarily to the rapid density fall-off with radius.

3.4.6. *M5*

Finally, M5 corresponds to a moderately more collimated jet, with $\xi = 5/8$. Again this results in a substantial change in the density and magnetic field structure, this time narrowing the jet. Unlike M4, the asymptotic Lorentz factor is also significantly altered, reaching only 3 in the region shown. Thus, the more rapid collimation results in a more slowly accelerating, narrow jet. This overproduces the extent of the 7 mm emission, and has difficulty producing the observed breadth.

4. JET IMAGES
4.1. 1.3 mm

Images of M87 at 1.3 mm (230 GHz) are presented in Fig. 5. As with images of accretion flows (Broderick & Loeb 2006a; Broderick et al. 2008), the outflow images are strongly influenced by relativistic beaming, boosting and strong gravitational lensing. In all images the jet is lopsided, with the emission dominated by the side in which the helically moving outflow is approaching the observer. However, whereas for accretion flows this results in a bright crescent, for our outflow model this produces a bifurcated image. This is clearly seen in the 1.3 mm image of M0, showing bright diagonal and vertical branches, which can be understood in terms of the generic velocity structure of the jet. As discussed in §3.4, the velocity is both largest and nearly radial along the critical magnetic field surface that divides the jet from the wind. Here, relativistic beaming dims the emission outside of a small angle, producing a flux deficit. Both inside and outside this surface, the toroidal component of the velocity increases, and the velocity is aligned along the line of sight, producing bright regions. The bright vertical and diagonal branches are due to emission from the jet and wind, respectively.

Even at a wavelength of 1.3 mm, the jet is typically not completely optically thin. This is not unexpected given that the jet spectrum is just turning over at 1.3 mm. This is most pronounced near the jet base, which obscures a portion of the black hole horizon. Nevertheless, in all images the silhouette cast by the black hole upon the lensed image of the base of the counter-jet[4] is clearly visible. This suggests that imaging a black hole silhouette may be more easily done in M87 than in Sgr A*. However, at 1.3 mm, the optimal beam, obtained by phasing together an array including all existing North American and European telescopes, the LMT and ALMA, is comparable in extent to the silhouette.

For the purpose of informing jet-formation modelling, it is fortuitous that each of the models is clearly distin-

guishable. The wider footprint of M1 results in a correspondingly broader brightness distribution. The lower velocities associated with lack of spin (M2) produces a featureless, asymmetric image with a single branch (though completely optically thin). Changing the inclination (M3) produces a broader base and narrower jet branch, though this case is most degenerate with the image from the canonical model (M0). It is not obvious whether images of the quiescent jet emission alone will distinguish these two cases. On the other hand, altering the collimation index even a small amount produces drastically different millimeter images (M4 & M5). Thus, short-wavelength imaging promises to severely constrain the jet footprint size, the black hole spin and the collimation index, all providing critical observational input into existing efforts to model the structure of MHD jets.

4.2. 0.87 mm

All of the features seen at 1.3 mm are also present at a wavelength of 0.87 mm (345 GHz). The two sets of images are subtly different primarily due to the decreased optical depth. Despite this, there are still optically thick regions for all models except M4. Again it is possible to clearly distinguish footprint size, black hole spin and collimation model. At 0.87 mm, the jet orientation is more easily discerned, though it remains unclear how accurately it may be determined.

Instead, most important is the reduction in the beam size relative to the horizon scale. At submillimeter wavelengths the black hole silhouette is now larger than the beam, implying that it is possible to clearly identify it in these images. However, comparison of the M4 image and the others suggests that it will not be possible to measure black hole spin with the silhouette detection alone, whose shape and size is similar for both high and low spins.

This is not unexpected since the primary effect of spin is to shift the silhouette. Unlike the horizon, the apparent silhouette size is insensitve to the spin magnitude. This can be easily see by considering critical orbits in the equatorial plane. The black hole silhouette is produced by geodesics which terminate on the horizon. For a non-rotating black hole, these correspond to impact parameters less than $\sqrt{27}GM/c^2 \simeq 5.2GM/c^2$, and thus a silhouette diameter of roughly $10.4\,GM/c^2$. For a rapidly rotating black hole, the critical impact parameter for prograde geodesics decreases. However, this is compensated for by the increase in the critical impact parameter of retrograde geodesics. In the case of a maximally rotating black hole ($a = 1$) these are $2\,GM/c^2$ and $7\,GM/c^2$, respectively. Thus the associated silhouette diameter has shrunk only to $9\,GM/c^2$, though it is shifted by roughly $2.2\,GM/c^2$ (see, e.g., Chandrasekhar 1992). As a result, efforts to discern the black hole spin by careful measurements of the silhouette size and shape alone are likely to be compromised by the rather large astrophysical uncertainties associated with the mass and distance to M87's black hole, as well as the resolution of future experiments.

5. JET POLARIZATION

Polarization maps for the six models we consider are shown in Fig. 7. The polarized flux can be comparable to the total flux, with the polarization fraction being

---

[4] In this case, we are seeing the counter-jet near to the black hole, where it has not yet accelerated appreciably and thus relativistic beaming is not yet effective. Far from the black hole the jet is rapidly moving away from the observer and beaming renders it invisible, as seen in Fig 3. Should the jet accelerate much more rapidly than modeled here, or the counter-jet not be present, the silhouette will be much weaker.
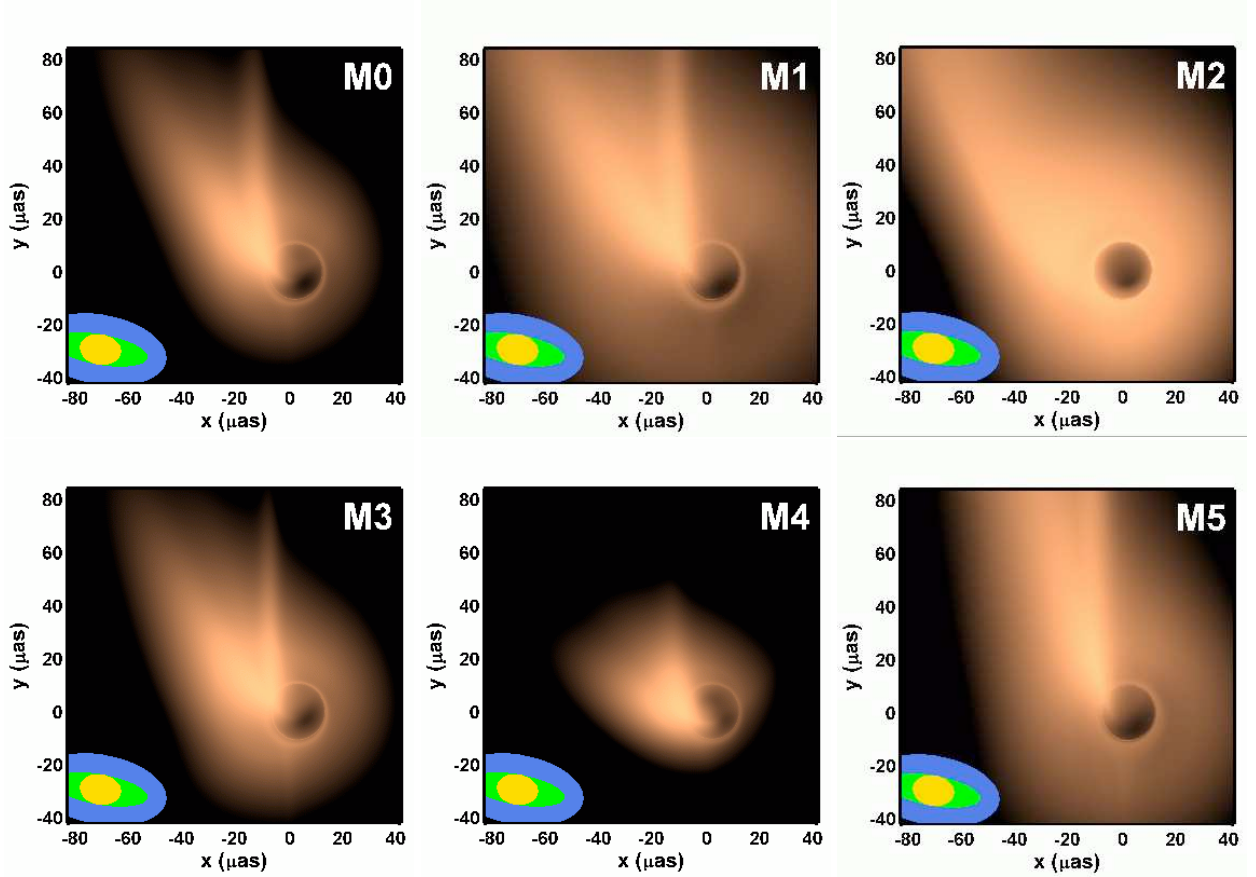
Fig. 6.— 0.87 mm (345 GHz) images for the models listed in Table 1 and described in §3.4. The brightness scale is logarithmic, showing a dynamic range of 128, similar to the existing 7 mm images. In all images the projected jet axis is parallel to the vertical axis. The ellipses in the lower left provide an estimate of the beam size for arrays consisting of the North American telescopes only (blue), including the European telescopes & the LMT (green), and all telescopes (yellow).

largest where the flux is greatest. As with earlier radio polarization studies, the polarization is indicative of the magnetic field structure, and in particular, the relationship between the plasma density and the magnetic field.

The maximum polarization fraction in all images is roughly 75%, is strongly correlated with the intensity, and thus should be relatively easily detected. The dominant magnetic field orientation is easily determined from the polarization maps in the usual way: assuming that the projected magnetic field direction is orthogonal to the polarization vectors. Unlike in some quasar jets (Lyutikov et al. 2005), the polarization angles here are not significantly altered by the relativistic motion. This is because of: (i) the moderate Lorentz factors in the regions contributing to the millimeter emission, and (ii) the orientation of the jet near the observer's line of sight. Most importantly, polarization measurements appear to provide a method by which the structure of the magnetic field lines may be compared directly with the collimation of the emitting plasma.

Since in our jet models the emitting electrons are relativistic, it is not possible to produce a robust estimate of the rotation measure (RM) from thermal electrons, and thus infer the importance of Faraday rotation for polarization measurements in M87. If there is a thermal population of electrons with a density comparable to the non-thermal component, we estimate a RM of roughly

10^6 rad m^{-2}, which produces a rotation in the plane of polarization at 1 mm of 60°. In this case, Faraday depolarization is unlikely to be a significant problem, and it will be possible to reconstruct the unrotated polarization map.

This should be tempered, however, by measurements of the rotation measure within M87's jet at longer wavelengths. At 20 mas from M87's core, the RM has been found to range from -4×10^3 rad m^{-2} to 10^4 rad m^{-2}, depending upon the location observed (Zavala & Taylor 2002). If these are not enhanced locally, due perhaps to a substantial over density of cold electrons within the knots being observed, they imply a rotation measure orders of magnitude higher near the black hole. That is, if $n \propto r^{-2}$ and $B \propto r^{-1}$, as expected at large distances, RM $\propto nBr \propto r^{-2}$. Extrapolating from 20 mas to 200 μas implies a nuclear RM of 10^8 rad m^{-2}, two orders of magnitude larger than our estimate. In this case, band-depolarization will still not be important for the largest bandwidths likely to be accessible (a few GHz). However, in situ Faraday depolarization will play a role, possibly attenuating the polarized flux considerably, depending upon geometric considerations. As such, the absence of polarization itself will constitute an interesting and potentially important constraint upon the non-relativistic electron population within M87's outflow.
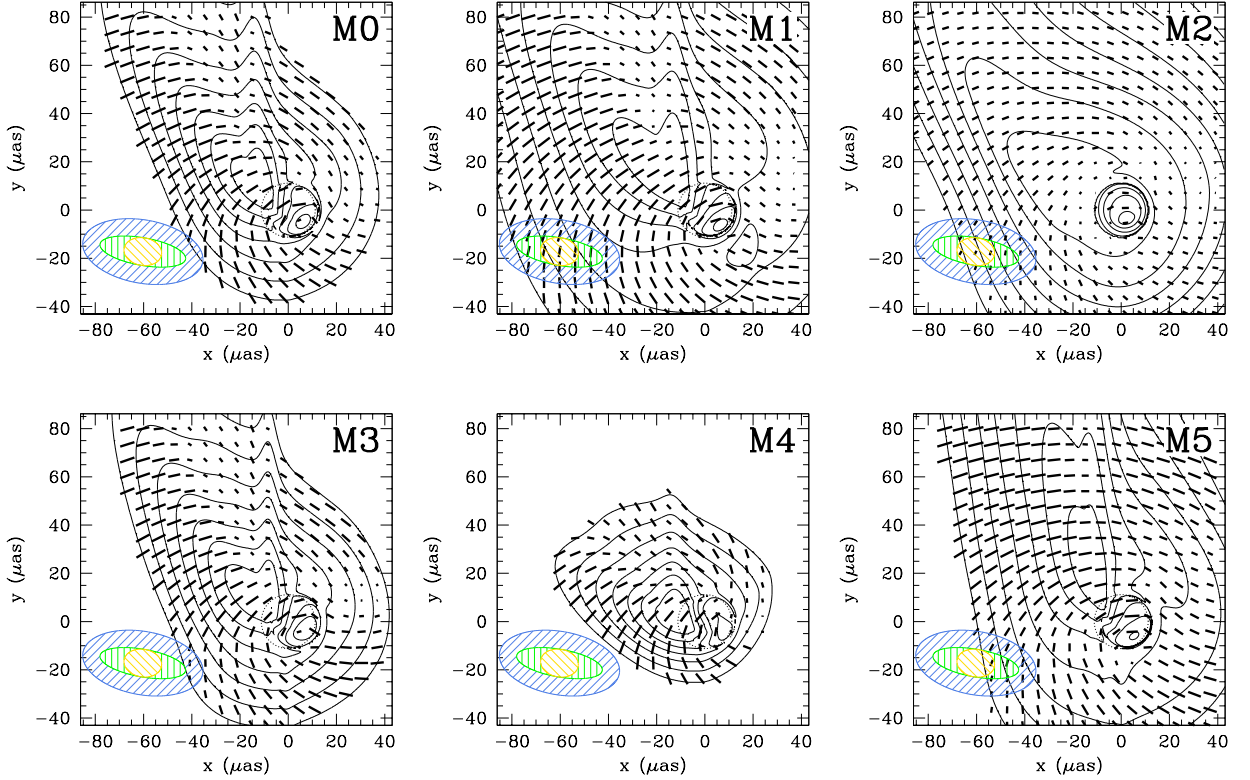
6. CONCLUSIONS

FIG. 7.— 0.87 mm (345 GHz) polarization maps of the models in Table 1, superimposed upon logarithmic contours of the intensity (factors of 2). The size of the tick marks are indicative of the polarization fraction, with the maximum polarization typically being 75%. The polarization vectors have not been Faraday rotated. The ellipses in the lower left provide an estimate of the beam size for arrays consisting of the North American telescopes only (blue), including the European telescopes & the LMT (green), and all telescopes (yellow).

M87 provides a promising second target for the emerging millimeter and submillimeter VLBI capability. Its presence in the Northern sky simplifies its observation and results in better baseline coverage than available for Sgr A*. In addition, its large black-hole mass, and correspondingly long dynamical timescale, makes possible the use of Earth aperture synthesis, even during periods of substantial variability.

Despite being dominated by a jet at millimeter wavelengths, the black hole silhouette, cast against the base of the counter-jet, is still clearly present, and may just be resolved at 0.87 mm (345 GHz). This requires that both the jet and the counter-jet are moving slowly near the black hole, and thus relativistic beaming does not preclude its observation. If, however, the counter-jet is either relativistic even at its base or simply not present the silhouette will not be detectable. Nonetheless, obtaining a sub-mm image of M87 appears to be more promising than efforts to image the silhouette of Sgr A* due to the lower opacity of the surrounding synchrotron emitting gas. Unfortunately, it is unlikely that the silhouette alone will be sufficient to constrain the spin without additional information. Better constraints may originate from exploring the effect of spin upon the jet image (via a change in the angular velocity profile of the jet footprint) or by carefully studying variability of hot spots in the accretion flow and jetted outflow. The latter possibility is feasible owing to the low optical depth to synchrotron self-absorption and the long dynamical timescales in M87.

Direct imaging of M87's jet on horizon scales will necessarily provide a wealth of information crucial to modern numerical efforts to model jet formation and propagation. In particular, such observations will be sensitive to the jet footprint size, collimation rate, and (if the jet is truly a magnetically dominated outflow) black hole spin. Polarized imaging will further shed light upon the structure of the jet's magnetic field and its relation to the emitting gas. Less well constrained will be the jet orientation.

Finally, comparisons of M87 and Sgr A* will provide the first opportunity to relate the gravitational properties of quasars, about which much is known, to the lower-mass, dormant black holes that LISA will access. Ultimately, such measurements will associate the black hole demographics measured by LISA with the existing, extensively studied set of known quasars.

APPENDIX

FORCE-FREE JET IN COVARIANT NOTATION

In order to perform the radiative transfer through the region around the M87 black hole we must characterize the surrounding plasma. This is done in terms of a proper density, n, a four-velocity, u^μ, and the magnetic field within the plasma frame $b^\mu \equiv u_\nu {}^*F^{\mu\nu}$, where ${}^*F^{\mu\nu}$ is the dual of the standard electromagnetic field tensor. Specifying that the magnetic field be force-free simplifies the definition of these quantities substantially. However, usually this is presented in a 3-dimensional vectors instead of the fully covariant form we require. In this appendix we review some relevant theorems and determine the jet structure in both notations.

Vector Force-Free Theorems

The "Force Free" condition is

$$\rho \mathbf{E} + \mathbf{j} \times \mathbf{B} = 0 \,, \tag{A1}$$

i.e., the Lorentz force vanishes. A direct consequence is that $\mathbf{E}$ and $\mathbf{B}$ are orthogonal:

$$\mathbf{B} \cdot (\rho \mathbf{E} + \mathbf{j} \times \mathbf{B}) = \rho \mathbf{B} \cdot \mathbf{E} = 0 \quad \Rightarrow \quad \mathbf{E} \cdot \mathbf{B} = 0 \,. \tag{A2}$$

This implies that there exists a frame in which one of these fields vanishes. For a force-free solution to exist we require that in this frame $\mathbf{E}$ vanishes, otherwise there would be no way to satisfy (A1) generally. Thus, the Lorentz scalar $B^2 - E^2$ must be non-negative. The velocity of this frame, called the "drift velocity" is not unique. However, we can define a class of such velocities:

$$\mathbf{v}_F = \frac{\mathbf{E} \times \mathbf{B}}{B^2} + \beta \mathbf{B} \quad \Rightarrow \quad \mathbf{E} = \mathbf{v}_F \times \mathbf{B} \,. \tag{A3}$$

Choosing β determines the frame in which we seek to define the drift velocity.

Maxwell's equations may be combined with the force-free condition to produce equations in which only the electromagnetic fields appear. For stationary solutions these give

$$\boldsymbol{\nabla} \cdot \mathbf{B} = 0 \,, \quad \boldsymbol{\nabla} \times \mathbf{E} = 0 \quad \text{and} \quad \mathbf{B} \times (\boldsymbol{\nabla} \times \mathbf{B}) = \mathbf{E} \boldsymbol{\nabla} \cdot \mathbf{E} \,, \tag{A4}$$

where the last of these arises directly from the force-free condition itself. This may be rewritten in terms of an unknown scalar function, α, as

$$\boldsymbol{\nabla} \times \mathbf{B} = \alpha \mathbf{B} + \mathbf{v}_F \boldsymbol{\nabla} \cdot \mathbf{E} \,, \tag{A5}$$

where α and $\beta \boldsymbol{\nabla} \cdot \mathbf{E}$ are degenerate. We shall refer to this second equation as the Force-Free equation.

Conserved Quantities

In axisymmetry, $\boldsymbol{\nabla} \times \mathbf{E} = 0$ implies that there can be no toroidal component to $\mathbf{E}$, and thus we may choose $\mathbf{v}_F$ to be purely toroidal as well. There are a number of immediate consequences. Firstly,

$$\mathbf{B} \cdot \boldsymbol{\nabla} \alpha = \boldsymbol{\nabla} \cdot \alpha \mathbf{B} = \boldsymbol{\nabla} \cdot (\boldsymbol{\nabla} \times \mathbf{B} - \mathbf{v}_F \boldsymbol{\nabla} \cdot \mathbf{E}) = 0 \,, \tag{A6}$$

and α is constant along poloidal magnetic field surfaces. Secondly, inspecting the poloidal components of the Force-Free equation (in spherical coordinates for convenience):

$$\sqrt{h} B^r = \frac{1}{\alpha} \partial_\theta B_\phi \quad \text{and} \quad \sqrt{h} B^\theta = -\frac{1}{\alpha} \partial_r B_\phi \,, \tag{A7}$$

where h is the determinant of the 3-metric, thus B_ϕ is constant along poloidal field surfaces as well. Coupled with the previous result for α, this implies that there exists a "stream function", $\psi \equiv \int \alpha^{-1} \mathrm{d}B_\phi$, which satisfies:

$$\sqrt{h} B^r = \partial_\theta \psi \quad \text{and} \quad \sqrt{h} B^\theta = -\partial_r \psi \,. \tag{A8}$$

Then, we can define $B_\phi(\psi)$ by its value on the equatorial plane (or any other convenient surface crossing every poloidal field line), which implicitly defines $\alpha(\psi) = \mathrm{d}\psi/\mathrm{d}B_\phi$. Thirdly, defining $\Omega \equiv v_F^\phi$, this implies:

$$\mathbf{E} = \Omega \boldsymbol{\phi} \times \mathbf{B} \quad \rightarrow \quad \boldsymbol{\nabla} \times \mathbf{E} = \boldsymbol{\phi} \mathbf{B} \cdot \boldsymbol{\nabla} \Omega = 0 \,, \tag{A9}$$

and thus Ω is constant along poloidal field surfaces as well. Note that for this choice of $\mathbf{v}_F$, there can be light-cylinders, a region where $v_F > c$. This does not mean that the Force Free condition has broken down. Rather, as we shall explicitly see in the jet models discussed below, the choice of $\mathbf{v}_F$ may simply be inappropriate. Nevertheless, the relationships between $\mathbf{E}$ and $\mathbf{B}$ are unchanged, and we may construct solutions that are continuous in the relevant observable quantities.

Determining the Stream Function

The stream function itself is determined from the phi-component of the Force-Free equation:

$$\left(1 - v^\phi v_\phi\right) \left(\partial_r \frac{g_{\theta\theta}}{\sqrt{h}} \partial_r \psi + \partial_\theta \frac{g_{rr}}{\sqrt{h}} \partial_\theta \psi\right) - \frac{v^\phi}{\sqrt{h}} \left[g_{\theta\theta} \left(\partial_r v_\phi\right) \left(\partial_r \psi\right) + g_{rr} \left(\partial_\theta v_\phi\right) \left(\partial_\theta \psi\right)\right] + \sqrt{h} B^\phi \frac{\mathrm{d}B_\phi}{\mathrm{d}\psi} = 0 \,. \tag{A10}$$

If we recast this relation in cylindrical coordinates, (R, z, ϕ), it reduces to

$$\left(1 - R^2\Omega^2\right) \partial_R^2 \psi + \left(1 - R^2\Omega^2\right) \partial_z^2 \psi - \left(1 + R^2\Omega^2\right) \frac{1}{R} \partial_R \psi - \Omega R^2 \frac{\mathrm{d}\Omega}{\mathrm{d}\psi} \left[\left(\partial_R \psi\right)^2 + \left(\partial_z \psi\right)^2\right] + B_\phi \frac{\mathrm{d}B_\phi}{\mathrm{d}\psi} = 0 \,, \tag{A11}$$

which, after trivial renamings, is identical to Eq. (13) in Narayan et al. (2007) (and also Okamoto 1974). All that remains is to specify, $\Omega(\psi)$, $B_\phi(\psi)$ and solve for ψ.

Vector Jet Structure

Here we use the various insights gained in the previous section to write down a qualitative jet model in covariant form. It is important to note that in both cases we are attempting only a qualitatively correct "solution", paying specific attention only to ensuring that the magnetic field geometry and the jet velocity do not become unphysical anywhere.

Following Tchekhovskoy et al. (2008), we begin by positing a class of stream functions based upon solutions to the $\Omega = 0$ stream-function equation:

$$\psi = r^p \left(1 - \cos\theta\right) . \tag{A12}$$

From this, we may immediately construct the poloidal magnetic field structure:

$$B^r = r^{p-2} \quad \text{and} \quad B^\theta = -pr^{p-3}\frac{1 - \cos\theta}{\sin\theta} = -pr^{p-3}\tan\frac{\theta}{2} . \tag{A13}$$

Since the toroidal component of the magnetic field scales as r^{-1}, far from the jet source it becomes electromagnetically dominated. Thus, $B^\phi B_\phi \simeq E^2 = R^2\Omega^2 B^r B_r$, and $B_\phi = -R^2\Omega B^r$, where the negative sign arises from the fact that the field lines are swept back (recall that $R = r\sin\theta$ is the cylindrical radius). That is,

$$B_\phi \simeq -r^2 \sin^2\theta\,\Omega\,r^{p-2} \simeq -2\Omega\psi . \tag{A14}$$

Therefore, since B_ϕ is conserved along magnetic field lines,

$$B^\phi = \frac{B_\phi(\psi)}{R^2} = -\frac{2\Omega(\psi)\psi}{r^2\sin^2\theta} = -2\Omega(\psi)r^{p-2}\frac{\tan(\theta/2)}{\sin\theta} . \tag{A15}$$

Thus, given $\Omega(\psi)$ (which we shall determine below), we now have the magnetic field value **B** everywhere.

Plasma Velocity

Because the plasma is non-relativistic initially, and the Bernoulli constant is conserved along the plasma flow, the plasma velocity is very similar to the drift velocity in the lab frame, and thus it is sufficient to compute the latter. The electric field in the lab frame is simply $\mathbf{E} = \Omega\boldsymbol{\phi} \times \mathbf{B}$. Therefore,

$$\mathbf{v} = \frac{\mathbf{E} \times \mathbf{B}}{B^2} = -\Omega\boldsymbol{\phi} + \frac{\Omega B_\phi}{B^2}\mathbf{B} \tag{A16}$$

Plasma Density

Finally, we must determine the electron/pair density in the jet. We do this assuming that the continuity equation holds, i.e., $\boldsymbol{\nabla} \cdot n\mathbf{v} = 0$. This is a dubious assumption for two reasons. First, if the mass-loading of the jet occurs over an extended region (e.g., if it is due to photon annihilation), then continuity fails locally. Second, and more severe, is that we are interested only in the nonthermal tail of the electron population. Thus, we might expect the electron acceleration process and cooling to leave an imprint upon the nonthermal electron distribution (which is completely ignored in our prescription). Nevertheless, in the absence of a more detailed understanding of jet formation, we proceed with this flawed working assumption, which gives,

$$\boldsymbol{\nabla} \cdot n\Omega\boldsymbol{\phi} + \boldsymbol{\nabla} \cdot n\frac{\Omega B_\phi}{B^2}\mathbf{B} = \mathbf{B} \cdot \boldsymbol{\nabla} n\frac{\Omega B_\phi}{B^2} = 0 , \tag{A17}$$

or $n\Omega B_\phi/B^2$ is constant along field lines. Since Ω and B_ϕ are already known to be constant along field lines, this gives $n \propto B^2$ along the field line. Thus, we must only specify n/B^2, i.e., the squared Alfvén velocity, at the jet footprint, finding

$$n = B^2 F(\psi) , \tag{A18}$$

everywhere else, for some function $F(\psi)$ that depends upon the jet loading at the footprint.

Covariant Force-Free Theorems

Each of the results in the previous sections can be presented in a fully covariant notation as well. In terms of the electromagnetic field tensor, the "Force Free" condition is

$$F^{\mu\nu}j_\nu = 0 . \tag{A19}$$

This also directly implies an orthogonality relation:

$${}^*F_{\sigma\mu}F^{\mu\nu}j_\nu = -\frac{1}{4}{}^*F_{\mu\nu}F^{\mu\nu}j_\sigma = 0 \quad \Rightarrow \quad {}^*F^{\mu\nu}F_{\mu\nu} = 0 , \tag{A20}$$

where we used the general relation ${}^*A^{\mu\nu}A_{\sigma\nu} = {}^*A^{\alpha\nu}A_{\alpha\nu}\delta^\mu_\sigma/4$ for all antisymmetric 2nd-rank tensors, $A^{\mu\nu}$ (which may be derived directly from the definition of the dual). This is not particularly surprising given that the Lorentz invariant ${}^*F^{\mu\nu}F_{\mu\nu} = 2\mathbf{E} \cdot \mathbf{B}$, where **E** and **B** are determined in the locally flat coordinate patch.

Again, we require that it is possible to transform into a frame in which the electric field vanishes, which corresponds to the condition that $F^{\mu\nu}F_{\mu\nu} \geq 0$. As before, the velocity of this frame is not uniquely defined, nor must it be physical.

However, if one such velocity is u_F^μ, then we require that the 4-vector that is coincident with **E** in this frame vanishes, i.e.,

$$e^\mu \propto u_F^\nu F_\nu^\mu = 0 \,. \tag{A21}$$

Thus, the acceptable u_F^μ comprise the null-space of F_ν^μ. Generally, given any u^μ we can write $F^{\mu\nu}$ and $*F^{\mu\nu}$ as

$$F^{\mu\nu} = u^\mu e^\nu - u^\nu e^\mu + \varepsilon^{\mu\nu\alpha\beta} u_\alpha b_\beta \quad \text{and} \quad *F^{\mu\nu} = u^\mu b^\nu - u^\nu b^\mu + \varepsilon^{\mu\nu\alpha\beta} u_\alpha e_\beta \,, \tag{A22}$$

where $\varepsilon^{\mu\nu\alpha\beta}$ is the Levi-Civita pseudotensor. If we set $u^\mu = u_F^\mu$, and thus $e^\mu = 0$, this implies that we can write these as

$$F^{\mu\nu} = \varepsilon^{\mu\nu\alpha\beta} u_{F\alpha} b_{F\beta} \quad \text{and} \quad *F^{\mu\nu} = u_F^\mu b_F^\nu - u_F^\nu b_F^\mu \,. \tag{A23}$$

Since we require that there *exists* a physical frame in which e^μ vanishes, there must be time-like choices for u_F^μ. This implies that the null space of $F^{m\nu}$ is two-dimensional with one time-like dimension and one space-like dimension (since $u_F^\mu b_\mu = 0$).

Since we know that $*F_\nu^\sigma F_\sigma^\mu = 0$ from the aforementioned orthogonality condition, the 4-vectors $v_{(\nu)}^\mu \equiv *F_\nu^\mu$ are necessarily components of $F^{\mu\nu}$'s null space. In fact, we can show that this space is completely spanned by the $v_{(\nu)}^\mu$, which are themselves degenerate. This may be proved by inspection, constructing a space-like and time-like basis vectors: $b_F^\nu *F_\nu^\mu = b_F^2 u_F^\mu$ and $u_F^\nu *F_\nu^\mu = u_F^2 b_F^\mu$ [5].

Regardless of the nature of u_F^μ, we may always construct time-like drift velocities. For any time-like vector, η^μ,

$$u^\mu = \frac{*F_\nu^\mu *F_\sigma^\nu \eta^\sigma}{\sqrt{-\eta_\gamma *F_\beta^\gamma *F_\alpha^\beta *F_\nu^\alpha *F_\sigma^\nu \eta^\sigma}} = \gamma (u_F^\mu + \beta b_F^\mu) \quad \text{where} \quad \beta \equiv \frac{u_F^2 \, b_F^\mu \eta_\mu}{b_F^2 \, u_F^\nu \eta_\nu} \quad \text{and} \quad \gamma \equiv -\frac{u_F^2}{\sqrt{-(u_F^2 + \beta^2 b_F^2)}} \,. \tag{A24}$$

Since the quantity u_F^2 appears in a number of places, let us define $\sigma = u_F^2 = \pm 1$. That η^μ be time-like itself is sufficient to guarantee that u^μ will be time-like as well. To see this, let us decompose η^μ into a tetrad basis with vectors $e_{(0)}^\mu = u_F^\mu$, $e_{(1)}^\mu \propto b_F^\mu$ and $e_{(2,3)}^\mu$ orthogonal to the rest (and thus necessarily space-like). Then,

$$u^2 \propto \eta^{(0)\,2} e_{(0)}^2 + \eta^{(1)\,2} e_{(1)}^2 \leq \eta^{(0)\,2} e_{(0)}^2 + \eta^{(1)\,2} e_{(1)}^2 + \eta^{(3)\,2} e_{(3)}^2 + \eta^{(3)\,2} e_{(3)}^2 = \eta^2 < 0 \,. \tag{A25}$$

Finally, we have chosen the arbitrary sign of u^μ such that it corresponds to forward-propagating particles. To see this generally, we again appeal to the tetrad expansion of η:

$$u^\mu \eta_\mu = \gamma (u_F^\mu \eta_\mu + \beta b_F^\mu \eta_\mu) = \frac{\gamma u_F^2}{u_F^\nu \eta_\nu} \left[\frac{(u_F^\mu \eta_\mu)^2}{u_F^2} + \frac{(b_F^\mu \eta_\mu)^2}{b_F^2} \right] = \frac{\gamma \sigma}{u_F^\nu \eta_\nu} \left(\eta^{(0)\,2} e_{(0)}^2 + \eta^{(1)\,2} e_{(1)}^2 \right) \,. \tag{A26}$$

Since the term in the parentheses is negative and we choose $u_F^\nu \eta_\nu$ to be negative by convention, this implies that γ must have the same sign as σ.

Note that if $\eta^\mu \propto u_F^\mu$, we find $u^\mu = u_F^\mu$. Thus, choosing η^μ is equivalent to choosing the frame in which we wish to define the drift velocity. That these are not all equivalent is a consequence of the ambiguity under boosts along the magnetic field. Nevertheless, if we are given a preferred frame (e.g., the lab frame) there is a unique definition, as in the 3-D vector computation. By inspection in the locally-flat coordinate frame we can show that this definition of u^μ is identical to the 3-D vector case.

We now turn to the various representations of the Force-Free equation. Recalling that Maxwell's equations give us $\nabla_\nu F^{\mu\nu} = 4\pi j^\mu$, the force-free condition may be trivially written in terms of $F^{\mu\nu}$:

$$F_\nu^\mu \nabla_\sigma F^{\nu\sigma} = 0 \,, \quad \text{or} \quad \nabla_\sigma F^{\mu\sigma} = \alpha b_F^\mu + \zeta u_F^\mu \,, \tag{A27}$$

i.e., once again we find that the vector we desire (in this case j^μ) is in the null-space of F_ν^μ. Now, there are two undefined functions, α which is analogous to the 3-D vector case, and ζ. As it turns out, we will be able to completely determine the magnetic field without ever having to specify ζ, which is not surprising given that there are only three independent components to b^μ.

Conserved Quantities

First, let us derive a number of useful relations in axisymmetry. As before, we shall assume that it is possible to put the field-line velocity (drift velocity) into a purely toroidal form by an appropriate boost along b_F^μ:

$$u_F^\mu = u_F^t t^\mu + u_F^\phi \phi^\mu \,, \tag{A28}$$

where t^μ and ϕ^μ are the time-like and azimuthal Killing vectors present in all stationary, axisymmetric spacetimes. The first thing we note is:

$$0 = b_{F\mu} \nabla_\nu *F^{\mu\nu} = b_{F\mu} \nabla_\nu (u_F^\mu b_F^\nu - b_F^\mu u_F^\nu) = b_F^\mu b_F^\nu \nabla_\nu u_{F\mu} \,, \tag{A29}$$

---

[5] Note that should we choose a form for u_F^μ that becomes space-like in some region, b_F^μ necessarily becomes time-like.

and thus the magnetic field must lie upon non-shearing velocity surfaces. This may be simplified by Killing's equation and the condition that $b_{F\mu}u_F^\mu = 0 \to b_{Ft} = -b_{F\phi}\Omega$ where $\Omega \equiv u_F^\phi/u_F^t$:

$$b_F^\mu b_F^\nu \nabla_\nu u_{F\mu} = b_F^\mu b_F^\nu \left(t_\mu \partial_\nu u_F^t + \phi_\mu \partial_\nu u_F^\phi\right) = b_{F\phi}b_F^\nu \left(\partial_\nu \Omega u_F^t - \Omega \partial_\nu u_F^t\right) = b_{F\phi}u_F^t b_F^\nu \partial_\nu \Omega. \tag{A30}$$

That is, Ω is constant along magnetic field lines.

Next we note

$$0 = u_{F\mu}\nabla_\nu {}^*F^{\mu\nu} = u_{F\mu}\nabla_\nu \left(u_F^\mu b_F^\nu - b_F^\mu u_F^\nu\right) = b_F^\mu u_F^\nu \nabla_\nu u_{F\mu} + \sigma \nabla_\nu b_F^\nu. \tag{A31}$$

The first term may again be simplified using Killing's equation:

$$\begin{aligned}
b_F^\mu u_F^\nu \nabla_\nu u_{F\mu} &= b_F^\mu u_F^\nu \nabla_\nu \left(u_F^t t_\mu + u_F^\phi \phi_\mu\right) \\
&= b_F^\mu \left(t_\mu u_F^\nu \partial_\nu u_F^t + \phi_\mu u_F^\nu \partial_\nu u_F^\phi + u_F^t u_F^\nu \nabla_\nu t_\mu + u_F^\phi u_F^\nu \nabla_\nu \phi_\mu\right) \\
&= -b_F^\mu \left(u_F^t u_F^\nu \nabla_\mu t_\nu + u_F^\phi u_F^\nu \nabla_\mu \phi_\nu\right) \\
&= b_F^\mu \left(t_\nu u_F^\nu \partial_\mu u_F^t + \phi_\nu u_F^\nu \partial_\mu u_F^\phi - u_F^\nu \nabla_\mu u_{F\nu}\right) \\
&= b_F^\mu \left(u_{Ft}\partial_\mu u_F^t + u_{F\phi}\partial_\mu u_F^\phi\right) \\
&= b_F^\mu \left(u_{Ft}\partial_\mu u_F^t + u_{F\phi}\partial_\mu \Omega u_F^t\right) \\
&= b_F^\mu \left[\left(u_{Ft} + u_{F\phi}\Omega\right)\partial_\mu u_F^t + u_{F\phi}u_F^t \partial_\mu \Omega\right] \\
&= \sigma b_F^\mu \partial_\mu \ln u_F^t.
\end{aligned} \tag{A32}$$

Therefore, $\nabla_\nu b_F^\nu = -b_F^\mu \partial_\mu \ln u_F^t$. However, from the Force-Free equation, we have

$$0 = \nabla_\mu \nabla_\nu F^{\mu\nu} = \nabla_\mu \alpha b_F^\mu + \nabla_\mu \zeta u_F^\mu = b_F^\mu \partial_\mu \alpha + \alpha \nabla_\mu b_F^\mu = b_F^\mu \partial_\mu \alpha - \alpha b_F^\mu \partial_\mu \ln u_F^t = u_F^t b_F^\mu \partial_\mu \frac{\alpha}{u_F^t}, \tag{A33}$$

and thus α/u_F^t is conserved along field lines.

This now brings us to the stream function. Again, looking at the poloidal parts of the Force-Free equation we find:

$$\begin{aligned}
\alpha b^r &= \varepsilon^{r\nu\alpha\beta}\partial_\nu u_{F\alpha}b_{F\beta} = \frac{1}{\sqrt{-g}}\partial_\theta \left(u_{F\phi}b_{Ft} - u_{Ft}b_{F\phi}\right) = -\frac{\sigma}{\sqrt{-g}}\partial_\theta \left(\frac{b_{F\phi}}{u_F^t}\right) \\
\alpha b^\theta &= \varepsilon^{\theta\nu\alpha\beta}\partial_\nu u_{F\alpha}b_{F\beta} = -\frac{1}{\sqrt{-g}}\partial_r \left(u_{F\phi}b_{Ft} - u_{Ft}b_{F\phi}\right) = \frac{\sigma}{\sqrt{-g}}\partial_r \left(\frac{b_{F\phi}}{u_F^t}\right),
\end{aligned} \tag{A34}$$

where we used

$$u_{Ft}b_{F\phi} - u_{F\phi}b_{Ft} = u_{Ft}b_{F\phi} + u_{F\phi}b_{F\phi}\frac{u_F^\phi}{u_F^t} = \frac{b_{F\phi}}{u^t}\left(u_{Ft}u_F^t + u_{F\phi}u_F^\phi\right) = \sigma \frac{b_{F\phi}}{u_F^t}. \tag{A35}$$

Since α/u^t is conserved along field lines, we may define a stream function by

$$\psi = \int \frac{u_F^t}{\alpha}\,\mathrm{d}\left(\frac{b_{F\phi}}{u_F^t}\right), \tag{A36}$$

which is very similar to the 3-D vector case, except for the presence of the u_F^t. In terms of this, we have

$$\frac{\sqrt{-g}}{u_F^t}b_F^r = -\sigma \partial_\theta \psi \quad \text{and} \quad \frac{\sqrt{-g}}{u_F^t}b_F^\theta = \sigma \partial_r \psi. \tag{A37}$$

Now the problem is again reduced to determining ψ.

Determining the Stream Function

At first glance, it may appear that we must also know ζ to obtain an equation for ψ. However, we can use the fact that $b_F^\mu u_{F\mu} = 0$ to avoid this requirement:

$$\begin{aligned}
\sqrt{-g}\alpha b_F^2 &= \sqrt{-g}b_{F\mu}\nabla_\nu F^{\mu\nu} = \sqrt{-g}\epsilon^{\mu\nu\alpha\beta}b_{F\mu}\partial_\nu u_{F\alpha}b_{F\beta} = \sqrt{-g}\epsilon^{\mu\nu\alpha\beta}b_{F\mu}u_{F\alpha}\partial_\nu b_{F\beta} \\
&= -\left(b_{Ft}u_{F\phi} - b_{F\phi}u_{Ft}\right)\left(\partial_r b_{F\theta} - \partial_\theta b_{Fr}\right) + b_{F\theta}\partial_r \left(\frac{b_{F\phi}}{u_F^t}\right) - b_{Fr}\partial_\theta \left(\frac{b_{F\phi}}{u_F^t}\right) \\
&\quad - b_{F\theta}\left(b_{Ft}\partial_r u_{F\phi} - b_{F\phi}\partial_r u_{Ft}\right) + b_{Fr}\left(b_{Ft}\partial_\theta u_{F\phi} - b_{F\phi}\partial_\theta u_{Ft}\right) \\
&= \sigma\sqrt{-g}\alpha\left(b_{Fr}b_F^r + b_{F\theta}b_F^\theta\right) + \sigma \frac{b_{F\phi}}{u_F^t}\left[\partial_r \frac{g_{\theta\theta}}{u_F^t \sqrt{-g}}\partial_r \psi + \partial_\theta \frac{g_{rr}}{u_F^t \sqrt{-g}}\partial_\theta \psi \right. \\
&\quad \left. - b_{F\theta}\left(u_F^\phi \partial_r u_{F\phi} + u_F^t \partial_r u_{Ft}\right) + b_{Fr}\left(u_F^\phi \partial_\theta u_{F\phi} + u_F^t \partial_\theta u_{Ft}\right)\right],
\end{aligned} \tag{A38}$$

where the following relations were used,

$$b_{Ft}\partial_i u_{F\phi} - b_{F\phi}\partial_i u_{Ft} = -\Omega b_{F\phi}\partial_i u_{F\phi} - b_{F\phi}\partial_i u_{Ft} = -\frac{b_{F\phi}}{u_F^t}\left(u_F^\phi\partial_i u_{F\phi} + u_F^t\partial_i u_{Ft}\right)$$

$$b_{F\theta}\partial_r\left(\frac{b_{F\phi}}{u_F^t}\right) - b_{Fr}\partial_\theta\left(\frac{b_{F\phi}}{u_F^t}\right) = \sigma\sqrt{-g}\alpha\left(b_{Fr}b_F^r + b_{F\theta}b_F^\theta\right) . \tag{A39}$$

Note also that

$$b_F^2 = b_{Ft}b_F^t + b_{F\phi}b_F^\phi + b_{Fr}b_F^r + b_{F\theta}b_F^\theta = b_{Fr}b_F^r + b_{F\theta}b_F^\theta + \frac{b_{F\phi}}{u_F^t}\left(u_F^t b_F^\phi - u_F^\phi b_F^t\right) , \tag{A40}$$

and thus,

$$\partial_r\frac{g_{\theta\theta}}{u_F^t\sqrt{-g}}\partial_r\psi + \partial_\theta\frac{g_{rr}}{u_F^t\sqrt{-g}}\partial_\theta\psi - \sigma b_{F\theta}\left(u_F^\phi\partial_r u_{F\phi} + u_F^t\partial_r u_{Ft}\right)$$

$$+ \sigma b_{Fr}\left(u_F^\phi\partial_\theta u_{F\phi} + u_F^t\partial_\theta u_{Ft}\right) + \sqrt{-g}\frac{\mathrm{d}\left(b_{F\phi}/u_F^t\right)}{\mathrm{d}\psi}\left(\frac{b_F^\phi}{u_{Ft}}\right) = 0 . \tag{A41}$$

This is quite similar to Eq. (A10), but significant differences remain. Most notably are the presence of various flow-velocity components (the u_F^t's). When $\Omega = 0$ this simplifies somewhat, though not as completely as in the 3-D vector case. The reason is that there may still be non-negligible terms due to gravity (i.e., non-vanishing derivatives of g_{tt}). In flat space, however, this gives precisely the same expression as Eq. (A10).

Covariant Jet Structure

Again, let us begin with the the class of stream functions,

$$\psi = r^p\left(1 - \cos\theta\right) . \tag{A42}$$

Furthermore, at each location we have u^t in terms of x^μ and $\Omega(\psi)$:

$$u_F^t = \left|g_{tt} + 2g_{t\phi}\Omega + g_{\phi\phi}\Omega^2\right|^{-1/2} . \tag{A43}$$

where some care has been taken to deal with the possibility of u_F^μ being space-like. We then determine the poloidal magnetic field seen by the orbiting observer as

$$b_F^r = -\sigma\frac{r^p\sin\theta}{u_F^t\sqrt{-g}} , \quad b_F^\theta = -\sigma p\frac{r^{p-1}(1-\cos\theta)}{u_F^t\sqrt{-g}}$$

$$b_{F\phi} = -2\Omega\psi\, u_F^t , \quad b_{Ft} = -b_{F\phi}\Omega \tag{A44}$$

All of these functions are well behaved in the region of interest. Note, however, that until we settle upon the plasma velocity, these results do *not* provide the magnetic field in the jet frame.

Plasma Velocity

Again, we assume that the plasma velocity is similar to the drift velocity as measured in some lab frame. Based upon the physical notion that zero-angular momentum gas should not see an acceleration along the jet (and guided by the requirement that we have a meaningful time-like vector), we choose

$$\eta_\mu = \left(-\frac{1}{\sqrt{-g^{tt}}}, 0, 0, 0\right) . \tag{A45}$$

As a result,

$$u^\mu = \gamma\left(u_F^\mu + \beta b_F^\mu\right) \quad \text{where} \quad \beta = \frac{\sigma b_F^t}{b_F^2 u_F^t} , \tag{A46}$$

and γ is given by Eq. (A24). In this frame, the magnetic field is

$$b^\mu = u_\nu\, {}^*F^{\mu\nu} = -u_\nu\sigma\left(u_F^\mu b_F^\nu - b_F^\mu u_F^\nu\right) = \gamma\left(b_F^\mu - \sigma b_F^2\beta u_F^\mu\right) , \tag{A47}$$

where the additional factor of $-\sigma$ is necessary to keep ${}^*F^{\mu\nu}$ continuous across the light cylinder[6].

---

[6] Up to now we did not need to worry about this since the overall sign of ${}^*F^{\mu\nu}$ did not matter

Plasma Density

Again, we set the density using the continuity equation. This gives

$$\nabla_\mu n u^\mu = \nabla_\mu n \gamma \left(u_F^\mu + \beta b_F^\mu \right) = \gamma \beta n \nabla_\mu b_F^\mu + b_F^\mu \partial_\mu \gamma \beta n = u_F^t b_F^\mu \partial_\mu \frac{\gamma \beta n}{u^t} = 0 \,. \tag{A48}$$

Thus, similar to the 3-D vector case, some combination of the magnetic field, Ω and the density is conserved along field lines. In Boyer-Lindquist coordinates, we can simplify β somewhat to bring this expression more in line with the 3-D vector case:

$$\beta = \frac{\sigma b_F^t}{b_F^2 u_F^t} = -\frac{\sigma b_F^\phi u_{F\phi}}{b_F^2 u_F^t u_{Ft}} = \frac{\sigma b_{F\phi} u_F^\phi}{b_F^2 u_F^t u_{Ft}} \left(g^{\phi\phi} - \Omega g^{t\phi} \right) \left(g_{\phi\phi} - \frac{g_{t\phi}}{\Omega} \right) = \sigma \left(\frac{b_{F\phi}}{u_F^t} \right) \Omega \frac{1}{b_F^2} \left(g^{tt} + \frac{1}{\Omega} g^{t\phi} \right) \,. \tag{A49}$$

The first two non-trivial factors, $b_{F\phi}/u_F^t$ and Ω, are conserved along field lines, which is very similar to the 3-D vector case. Therefore,

$$b_F^\mu \partial_\mu \left[\frac{\gamma n}{u_F^t b_F^2} \left(g^{tt} + \frac{g^{t\phi}}{\Omega} \right) \right] = 0 \,, \tag{A50}$$

is conserved along field lines. That is, the density is given by

$$n = \frac{u_F^t b_F^2}{\gamma} \left(g^{tt} + \frac{g^{t\phi}}{\Omega} \right)^{-1} F(\psi) \tag{A51}$$

given the arbitrary function $F(\psi)$. This is chosen as described in the main text.

Parameters & Summary

As before we must set three parameters (the power-law index p and the density & magnetic field normalizations) and two functions of ψ ($\Omega(\psi)$ and $F(\psi)$). We describe how these are chosen in the main text. Given these, in practice the procedure for computing the magnetic field, plasma velocity and plasma density at a point x^μ is:

1. Settle upon p, $\Omega(\psi)$ and $F(\psi)$.

2. Construct $b_F(x^\mu)$ and $u_F^t(x^\mu)$.

3. From these, construct $b^\mu(x^\mu)$, $u^\mu(x^\mu)$ and $n(x^\mu)$.

REFERENCES

Biretta, J. A., Stern, C. P., & Harris, D. E. 1991, AJ, 101, 1632
Bower, G. C. et al. 2006, ApJL, 648, L127
Broderick, A. & Blandford, R. 2004, MNRAS, 349, 994
Broderick, A. E. & Loeb, A. 2005, MNRAS, 363, 353
Broderick, A. E. & Loeb, A. 2006a, ApJL, 636, L109
Broderick, A. E. & Loeb, A. 2006b, MNRAS, 367, 905
Broderick, A. E. et al. 2008, ApJ (*submitted, arXiv:0809.4490*)
Chandrasekhar, S. 1992, The mathematical theory of black holes (New York : Oxford University Press, 1992.)
De Villiers, J.-P., Hawley, J. F., & Krolik, J. H. 2003, ApJ, 599, 1238
De Villiers, J.-P., Hawley, J. F., Krolik, J. H., & Hirose, S. 2005, ApJ, 620, 878
Despringre, V., Fraix-Burnet, D., & Davoust, E. 1996, A&A, 309, 375
Doeleman, S. 2008, J. Phys. Conf. Series, 131, 012055
Doeleman, S. S. et al. 2008a, Nature, 455, 78
Doeleman, S. S. et al. 2008b, ApJ (*submitted, arXiv:0809.3424*)
Falcke, H., Melia, F., & Agol, E. 2000, ApJL, 528, L13
Hawley, J. F. & Krolik, J. H. 2006, ApJ, 641, 103
Heinz, S. & Begelman, M. C. 1997, ApJ, 490, 653
Igumenshchev, I. V. 2008, ApJ, 677, 317
Jones, T. W. & Odell, S. L. 1977, ApJ, 214, 522
Junor, W., Biretta, J. A., & Livio, M. 1999, Nature, 401, 891
Komissarov, S. S. 2005, MNRAS, 359, 801
Kovalev, Y. Y., Lister, M. L., Homan, D. C., & Kellermann, K. I. 2007, ApJL, 668, L27
Krichbaum, T. P. et al. 2006, J. Phys. Conf. Series, 54, 328
Ly, C., Walker, R. C., & Wrobel, J. M. 2004, AJ, 127, 119
Lyutikov, M., Pariev, V. I., & Gabuzda, D. C. 2005, MNRAS, 360, 869

Marscher, A. P. et al. 2008, Nature, 452, 966
McKinney, J. C. 2006, MNRAS, 368, 1561
McKinney, J. C. & Gammie, C. F. 2004, ApJ, 611, 977
Mills, A. P. 1962, The Appearance of Spherically Symmetric Objects with Radius Comparable to $2mG/c^2$, Senior Thesis, supervised by C. Misner & J. A. Wheeler, Princeton University
Miyoshi, M. et al. 2007, Publ. Natl. Astron. Obs. Japan, 10, 15
Narayan, R., McKinney, J. C., & Farmer, A. J. 2007, MNRAS, 375, 548
Nishikawa, K.-I. et al. 2005, ApJ, 625, 60
Okamoto, I. 1974, MNRAS, 167, 457
Perlman, E. S. et al. 2001, ApJL, 561, L51
Perlman, E. S. et al. 2007, ApJ, 663, 808
Petrosian, V. & McTiernan, J. M. 1983, Phys. of Fluids, 26, 3023
Reynolds, C. S., di Matteo, T., & Fabian, A. C. 1999, in Lecture Notes in Physics, Berlin Springer Verlag, Vol. 530, The Radio Galaxy Messier 87, ed. H.-J. Röser & K. Meisenheimer, 313–+
Tan, J. C. et al. 2008, ApJ(*accepted*)
Tchekhovskoy, A., McKinney, J. C., & Narayan, R. 2008, MNRAS, 388, 551
Walker, R. C., Ly, C., Junor, W., & Hardee, P. J. 2008, J. Phys. Conf. Series, 131, 012053
Yuan, F. 2000, MNRAS, 319, 1178
Yuan, F., Quataert, E., & Narayan, R. 2003, ApJ, 598, 301
Zavala, R. T. & Taylor, G. B. 2002, ApJL, 566, L9